Supporting Information

Macro- and Micro-scale Investigation of Selenium Speciation in Blackfoot River, Idaho, USA Sediments

Libbie L. Oram, Daniel G. Strawn, Matthew A. Marcus, Sirine C. Fakra, and Gregory Möller

No. of pages in Supporting Information Section: 20

No. of tables in Supporting Information Section: 3

No. of figures in Supporting Information Section: 9

Additional Materials and Methods

Sampling. The water samples were acidified in the field with nitric acid (HNO_3). Sediment sampling was accomplished using a slide-hammer corer (Halltech Environmental, Guelph, Ontario) fitted with a T-handle. The core tubes are polycarbonate, 7.5 cm I.D., 125 cm in length, and have a wall thickness of 1.6 mm. Each sampling location was approached from downstream to minimize contamination from disturbed, suspended sediment and sampling gear. The specific location for sampling was selected in an apparent depositional zone.

Selenium Analysis. USEPA method 3050 was used to digest and analyze the sediment cores to measure total Se at each depth interval (*1*). The method detection limit was 0.75 mg Se kg^{-1} sediment. Each water sample and digest solution was analyzed for total Se using USEPA method 200.8 with an Agilent 7500c ICP-MS, monitoring Se mass lines m/z 77, 78, and 82. An internal standard of 50 µg L^{-1} germanium, tellurium, and yttrium was used, and the instrument was calibrated using Spex CertiPrep (Metuchen, NJ) standards, traceable to NIST. The UIASL analysis QA/QC protocol includes blanks, standards, fortifications and standard reference materials. The method detection limit for Se is 1 µg Se L^{-1}.

Sequential Extractions. Following the protocol in Kulp and Pratt (*2*) and other research (*3-6*), each sample was air dried overnight at 40°C and ground. A portion was submitted for total Se analysis as described above, while a separate 1.5 g subsample was weighed into centrifuge tubes, to which 25 mL of the extracting solution of the current extraction step was added. After shaking for a given time period (2 h for water, 2 h for P-buffer, 2 h for sodium hydroxide, 8 h ultrasonic bath for sodium sulfite, and 2 h for acetic acid), the samples were centrifuged and the supernatant decanted and filtered through a 0.2 µm membrane for Se analysis. The subsequent extracting solution was added to the pellet, and after each extraction, the pellets were rinsed with 10 mL reagent water before adding the solution for the next

step. Except for the sulfite extraction, the supernatant solutions from each extraction were analyzed via ICP-MS as described. Due to interferences with sulfur, the supernatant from the sulfite extraction was analyzed via Hydride Generation - Atomic Fluorescence Spectroscopy using a Millennium Excalibur-System, PSA 10.055 (PS Analytical Ltd, Kent, United Kingdom). The instrument was equipped with a Phototron Superlamp (Phototron Pty. Ltd., Victoria, Australia) Se super hollow cathode lamp and calibrated using Spex CertiPrep (Metuchen, NJ) standards. The reductant used to generate selenium hydride was a solution of sodium borohydride ($NaBH_4$) and sodium hydroxide (NaOH), and argon was the carrier gas. The instrument detection limit is 2 ng Se L^{-1}.

X-ray Spectroscopy. Waypoint 04 and WP 09 samples were selected for μ-SXRF based on total Se content, where higher concentrations allow more efficient μ-SXRF data collection, and respective upstream and downstream location. Small portions (less than 0.25 g) of frozen sediment samples were slightly thawed at room temperature for 15-30 seconds and gently smeared onto a silver plate on a Peltier cooler, which was attached to an XYZ stage oriented at 45° to the beam. The Peltier cooler was used to keep the samples frozen to inhibit radiation damage of the sample. For μ-SXRF mapping, the beam was focused to 7 μm x 7 μm, with a dwell time of 200 ms per pixel and a step size of 20 μm x 20 μm. Because the step size was larger than the beam size, each 20 μm x 20 μm pixel in an XRF image represents an average of the Se signal over a 20 μm x 7 μm swath.

For Se species identification, μ-SXRF maps were deconvoluted for signal overlap according to the method of Sutton et al. (*7*) as follows: XANES absorption intensities at E1, E2, and E3 were taken from the three normalized XANES spectra for Se(-II, 0), Se(IV), and Se(VI) (gray orthorhombic elemental Se, sodium selenite, and sodium selenate (Aldrich Chemical Co.)). We therefore had nine normalized intensity reference compound values (S_{ij}) to define matrix S:

$$S_{ij} = \begin{bmatrix} S_{11} & S_{12} & S_{13} \\ S_{21} & S_{22} & S_{32} \\ S_{31} & S_{32} & S_{33} \end{bmatrix} \quad \text{……..…1}$$

Each row (*i*) in the matrix represents a different standard, and each column (*j*) a different energy. In each energy map, every pixel was normalized by subtracting the below edge fluorescence (12608.0 eV) and dividing by the Se edge +100 (12778.0 eV) energy fluorescence, resulting in a normalized pixel intensity map, defined as *F*:

$$F_j = \begin{pmatrix} F_1 & F_2 & F_3 \end{pmatrix} \quad \text{……...……2}$$

The theoretical oxidation state fractions (X) at each pixel for Se(0), Se(IV), and Se(VI), make up vector *X*:

$$X_i = \begin{pmatrix} X_1 & X_2 & X_3 \end{pmatrix} \quad \text{……...……3}$$

X_1 is the fraction of Se(-II, 0), X_2 is the fraction of Se(IV), and X_3 is the fraction of Se(VI). At each pixel the total fluorescence at each of the energies can be computed by,

$$F = XS \quad \text{……..4}$$

Solving for *X*, which is the pure fraction of Se species at a given pixel, by multiplication on the right by S^{-1},

$$X = FS^{-1} \quad \text{…….5}$$

where the sum of X1, X2, and X3 equal 1 when the signal is normalized. Therefore, to obtain the signal-corrected data X=([Se(-II,0)],[Se(IV)],[Se(VI)]), at each pixel, we multiply the *F* vector by the inverted *S* matrix at each sample position in the map.

Additional Results and Discussion

Total organic carbon in the sediments ranged from 1.3 – 3.1%, and particle size ranged from 32 – 72% sand, 22 – 54% silt, and 6 – 14% clay. No significant correlations were observed between organic carbon content or particle size and operationally-defined Se speciation.

Sequential Extractions. The sediment samples are relatively low in Se concentration with respect to analytical detection limits and experimental error. Thus small errors in accuracy and precision that are otherwise normal can translate into large variation in Se recovery. Despite these analytical challenges, it is important to analyze samples with low concentrations because Se can be toxic at relatively low levels. The difference between the total Se recovered from the pooled sequential extraction steps and the total Se measured independently was 2-61% of the total, with an average of 35% (n=10). Differences are due to loss during fractionation steps and Se concentrations in extracted solution near or below analytical detection limits. A smaller-scale second experiment on samples 04A and 09A was conducted to verify interpretations and/or reconcile the loss of Se. Results showed excellent recovery (98 - 104%) when the NaOH extract was not acidified prior to introduction in the auto sampler, but acidified directly in-line before injection into the ICP-MS plasma, *and* when Se concentrations in all of the extracted solutions were above analytical detection limits (1 μg Se L^{-1}). Most importantly, the second extraction experiment confirmed that all interpretations from the first sequential extraction experiment were correct.

Air drying and grinding of samples may also introduce artifacts due to oxidation of reduced, immobile species to more soluble phases. However, Martens and Suarez (*8*) showed that air-drying of samples for 48 hours will not substantially alter the distribution of soil Se oxidation states. Furthermore, mobile, oxidized Se is measured in the first two steps in the extraction procedure, and results indicate that these fractions are minor (<14% of the total Se). Thus, oxidation due to air drying and grinding did not cause a significant increase in extractable Se species.

X-ray Spectroscopy. The accuracy of defining a species using energy dependent mapping is affected by several factors, including: variability in matrix effects, over-absorption, Se speciation (e.g., two different Se species with the same oxidation state may have different spectral features, including maxima and minima), and inconsistencies between signal intensities from pure standards and those emitted from a natural sample. As a result of these unknown factors, it is not possible to calculate an exact S matrix for these samples. Therefore, because of the experimental overlap in Se species inherent in natural samples, we are limited to assigning general categories for Se speciation. For example, the selenide and elemental Se compounds have varying white line positions, ranging from 12659 eV to 12662 eV (between that for Se(0) and Se(IV) species) (*9*), making refinement of the different reduced species difficult. Despite the large white-line energy range for reduced Se compounds, the relative intensity of metal selenide minerals, organic selenide compounds, and elemental Se is two to six times the intensity of Se(IV) at E1 (*10*). In our approach, the signal deconvolution algorithm is precise and accurate for categorizing Se into reduced Se (i.e., selenides and elemental Se), Se(IV), and Se(VI) oxidation states.

Radiation-induced reduction is not expected to be an artifact in these μ-SXRF maps because of the short beam dwell time at each pixel. Radiation damage was monitored at the ALS by collecting successive XANES scans of selenate standard before collecting oxidation state maps. In addition, Ryser et al. (*11*) measured kinetics of radiation-induced reduction by collecting successive, five-minute XANES scans of selenate adsorbed on goethite and observed no radiation damage after the first five minute scan for soil samples.

To more clearly illustrate oxidation state variability and the effects of processing the data according to the protocol described above (equations 1 – 5), raw and processed data from three transects are shown in Figures S3, S5, S7, and S9. The correlations between species before signal deconvolution

suggests that there is significant signal cross-contamination between the three energies (e.g., see Figure S3). The processed data shows that much of the correlation between the three energies is removed after signal deconvolution. Thus the resulting signal at each pixel is more representative of the relative species contribution. We can make general interpretations from the raw data, but because the intensity of the Se signal has significant overlap from fluorescence of other species, it is necessary to process the data to draw accurate conclusions and allow the data to be visualized in the micrographs. The transect data confirms results from visual interpretations of the oxidation state micrographs.

The XRF spectrum from a point of interest (POI) (arrow in Figure S2) in sample 04A is shown. The Kα1 peak for Se is at 11,224 eV. Iron fluorescent peaks (Kα1 = 6,405 eV and Kβ1 = 7,059 eV) predominate in the spectrum. Other peaks present are Ag (Lα1=2983 eV), Ca (Kα1=3,692 eV), Ti (Kα1=4,512 eV), Cu (Kα1=8,046 eV), and Zn (Kα1=8,637 eV). XRF spectra for samples 04G, 09A, and 09C show similar components at various Se hotspots.

X-ray fluorescence for carbon cannot be measured at beamline 10.3.2, and sulfur cannot be reliably measured under the same instrument parameters used for Se X-ray absorbance measurement. Therefore, spatial correlation with carbon or sulfur could not be directly determined.

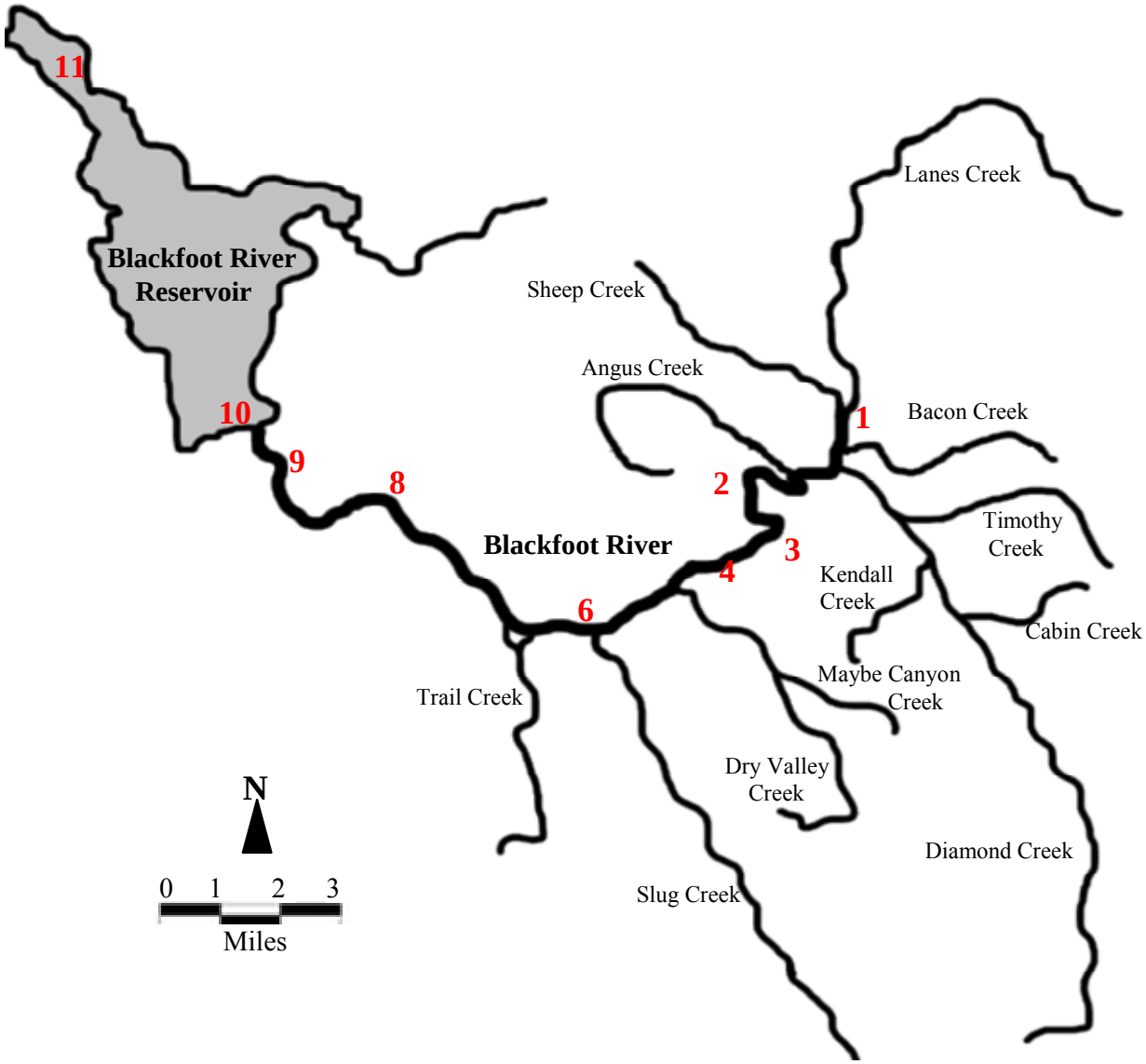

Figure S1. Rivers and streams of the upper Blackfoot River watershed, Caribou County, Idaho, USA. Adapted from Idaho DEQ (*12*). Waypoints sampled are marked with a red number, starting with the east most waypoint 1, 2, 3, 4, 6, 8, 9, 10, and ending with the west most waypoint, 11.

Table S1. Total Se (μg L^{-1}) in the Blackfoot River at waypoints sampled during three sampling events, September 2004 (Sep-04), June 2005 (Jun-05), and August 2005 (Aug-05).

Waypoint	*Sep-04*	*Jun-05*	*Aug-05*
1	<1.0	<1.0	<1.0
2	<1.0	1.4	1.4
3	<1.0	1.1	1.4
4	<1.0	1.3	1.6
6	<1.0	1.2	1.2
8	<1.0	1.1	<1.0
9	<1.0	1.2	<1.0
10	<1.0	1.3	<1.0
11	1.4	<1.0	<1.0

Table S2. Total Se (μg g^{-1}) in BFR sediments at nine waypoints at each depth sampled for three sampling events, September 2004, June 2005, and August 2005.

	WPT01			**WPT02**			**WPT03**		
Depth (cm)	*Sep-04*	*Jun-05*	*Aug-05*	*Sep-04*	*Jun-05*	*Aug-05*	*Sep-04*	*Jun-05*	*Aug-05*
1-3	1.1	0.8	<0.75	3.7	1.3	1.3	5.0	2.7	1.0
4-6	0.8	1.2	<0.75	2.8	1.4	1.0	4.9	2.6	<0.75
7-9	0.8	1.0	0.8	1.0	1.0	1.7	4.2	2.4	<0.75
10-12	0.8	1.4	0.8	1.6			4.1		0.8
13-15	0.8		0.8	1.1					2.3
16-18	0.8		0.9	1.2					3.4
19-21			<0.75	1.0					4.1
22-24									3.2
25-27									3.5
28-30									1.5
	WPT04			**WPT06**			**WPT08**		
Depth (cm)	*Sep-04*	*Jun-05*	*Aug-05*	*Sep-04*	*Jun-05*	*Aug-05*	*Sep-04*	*Jun-05*	Aug-05
1-3	5.0	3.2	4.3	3.0	3.3	3.2	3.0		2.6
4-6	4.4	3.9	3.6	2.7	3.7	1.9	3.9		3.4
7-9	5.5	3.0	2.3	<0.75	4.0	1.5	3.4		3.3
10-12	2.1	1.5	5.3	<0.75	3.0	1.1	2.9		
13-15	2.4	1.1	3.9	<0.75	1.4	1.9	2.3		
16-18	1.3	1.5	4.1	1.1	1.6	3.4	2.2		
19-21			4.0			3.6	3.3		
22-24			5.4			2.5	2.1		
25-27						2.0			
28-30						2.2			
	WPT09			**WPT10**			**WPT11**		
Depth (cm)	*Sep-04*	*Jun-05*	*Aug-05*	*Sep-04*	*Jun-05*	*Aug-05*	*Sep-04*	*Jun-05*	*Aug-05*
1-3	2.2	2.7	2.5	<0.75	1.9	2.6	1.2	1.1	<0.75
4-6	1.6	2.2	2.2	<0.75	1.9	1.1	1.4	1.1	0.8
7-9	1.4	2.6	3.6	<0.75	1.3	1.2	1.6	1.1	0.8
10-12	1.5	1.8	2.4	<0.75	1.1	<0.75	1.3	1.2	0.9
13-15		2.1	4.6	<0.75	2.0	1.4	1.5	0.9	
16-18				<0.75	2.1	1.4	1.4	1.9	
19-21					1.2	1.8	0.8	1.3	
22-24					2.0	1.3	<0.75	1.6	
25-27					1.5		<0.75		
28-30					2.1		<0.75		
31-33					2.0		<0.75		
34-36					1.8		<0.75		

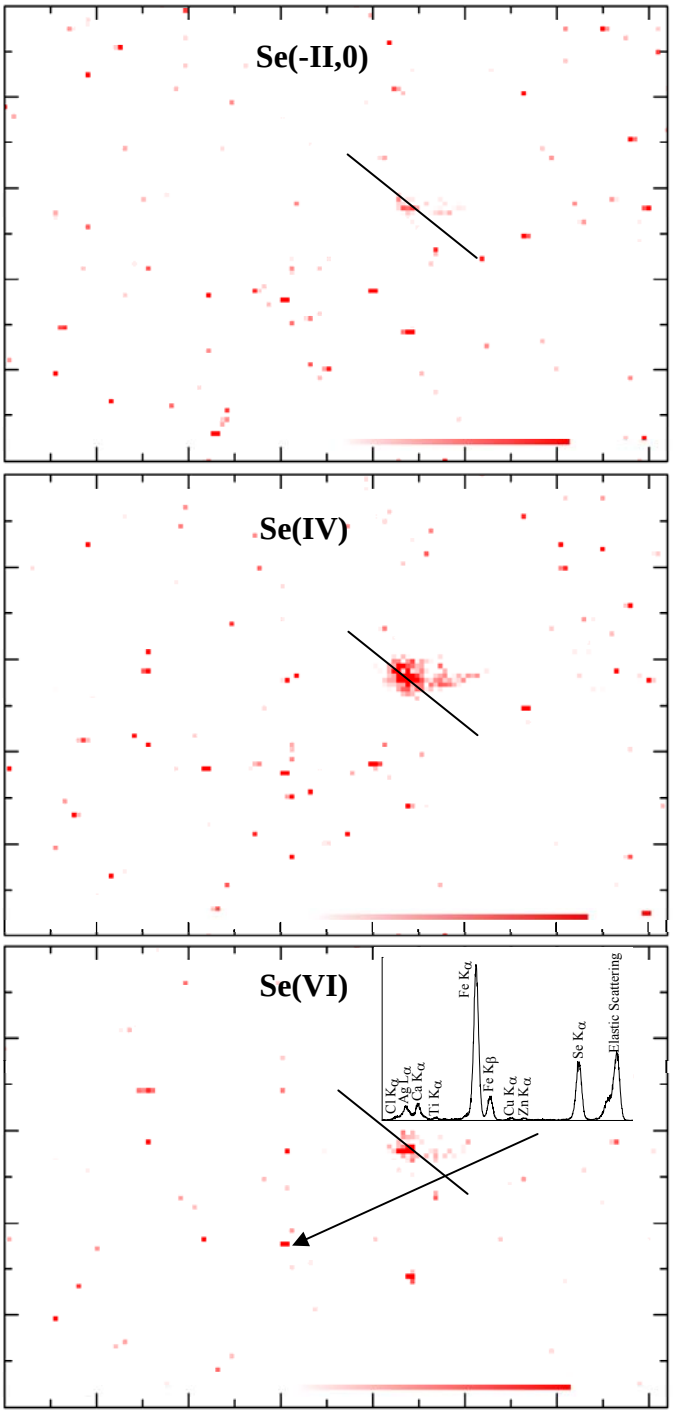

Figure S2. Micro-SXRF maps of sample 04A, 2880 x 2000 µm. Each pixel shows deconvoluted signal (X in equation 3). Se(-II,0) map was collected at 12659.0 eV, Se(IV) at 12663.5 eV, and Se(VI) at 12668.5 eV. Red to white gradient shows decreasing Se levels. An XRF spectrum of a Se hotspot is also shown. The black line is a transect line for which the data is shown in Figure S3.

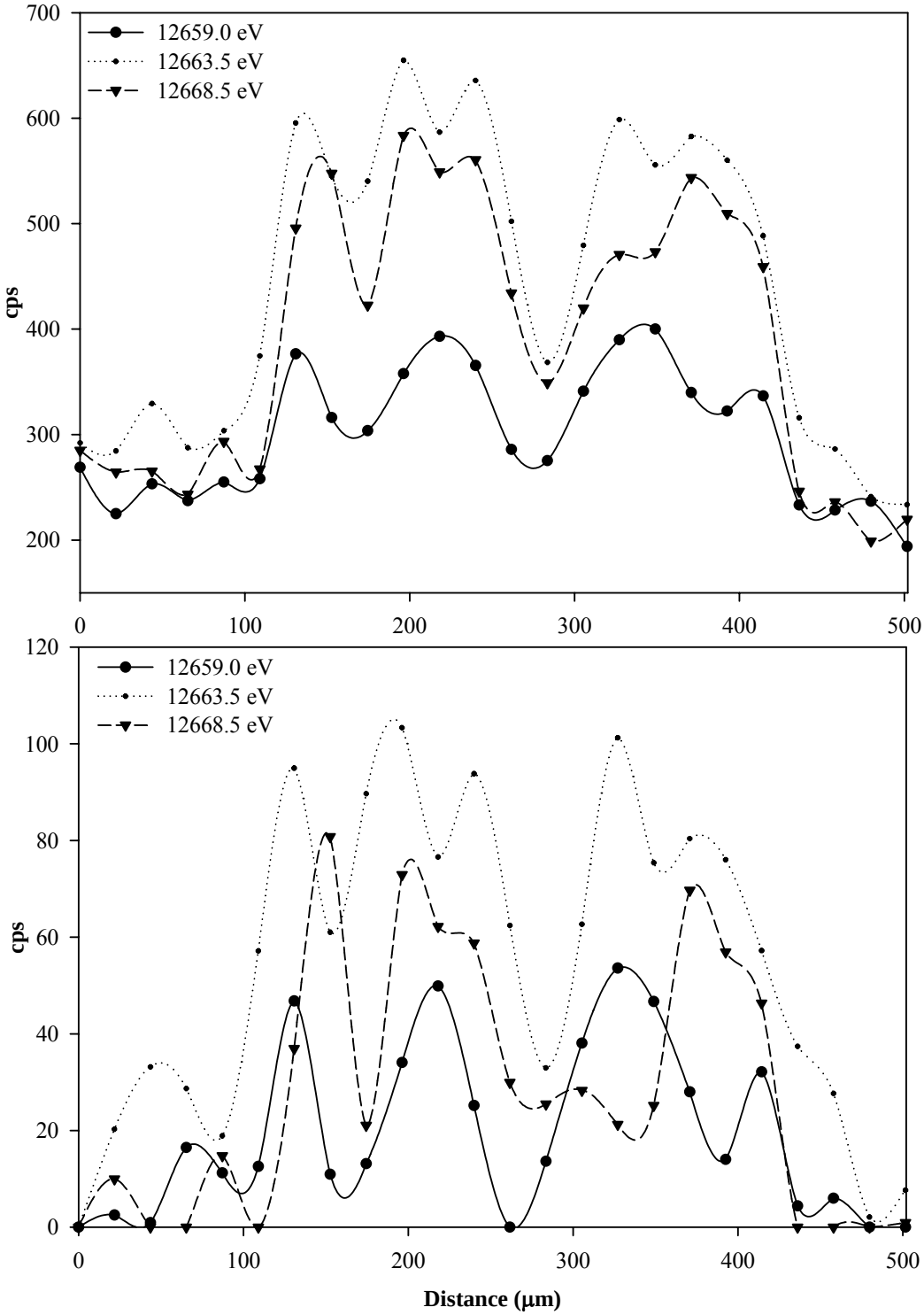

Figure S3. (top) Raw SXRF data (F in equations 4-5) from transect of sample 04A at three energies. (bottom) Signal interference-corrected SXRF data (X in equations 4-5) from transect of sample 04A at three energies. Upper left to lower right of transect correlates with left to right on plot.

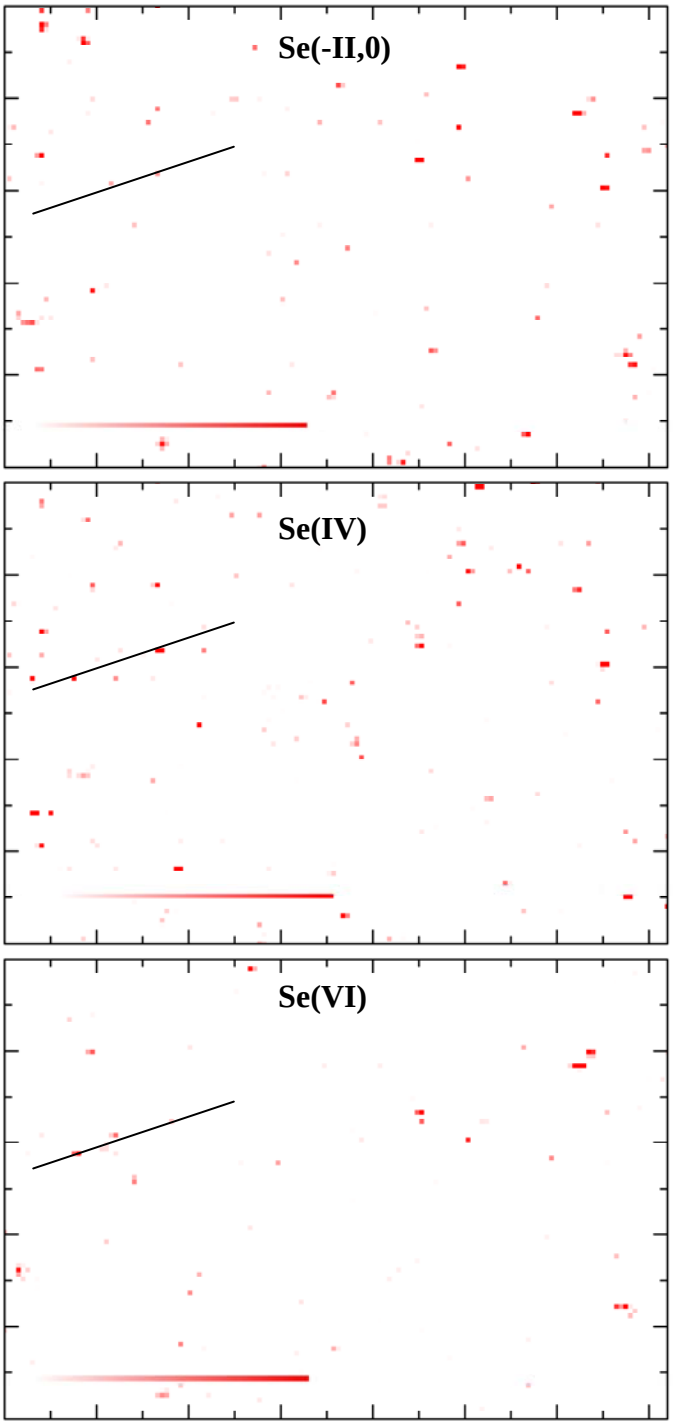

Figure S4. Micro-SXRF maps of sample 04G, 2880 x 2000 µm. Each pixel shows deconvoluted signal (X in equation 3). Se(-II,0) map was collected at 12659.0 eV, Se(IV) at 12663.5 eV, and Se(VI) at 12668.5 eV. Red to white gradient shows decreasing Se levels. The black line is a transect line for which the data is shown in Figure S5.

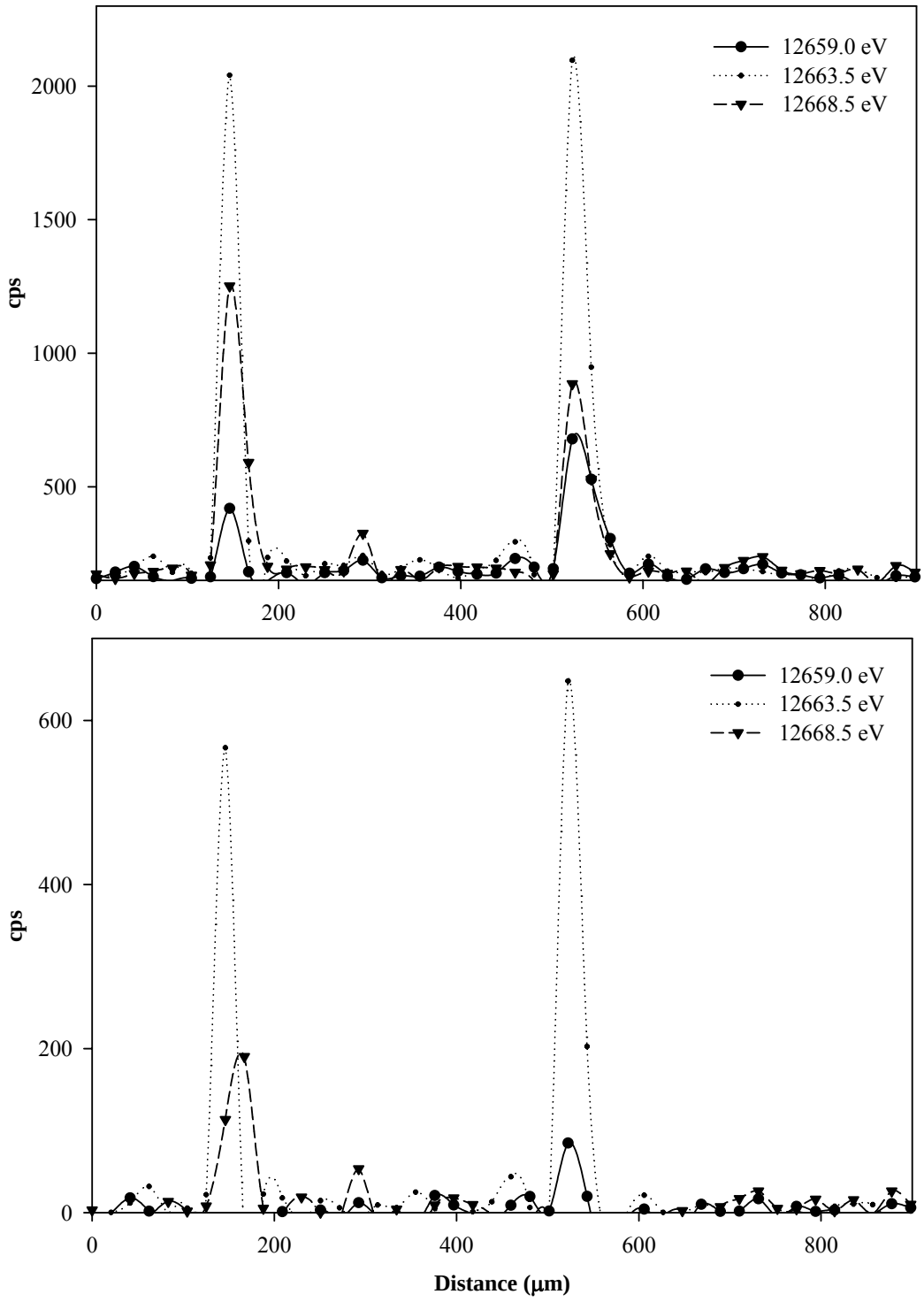

Figure S5. (top) Raw SXRF data (F in equations 4-5) from transect of sample 04G at three energies. (bottom) Signal interference-corrected SXRF data (X in equations 4-5) from transect of sample 04A at three energies. Lower left to upper right of transect correlates with left to right on plot.

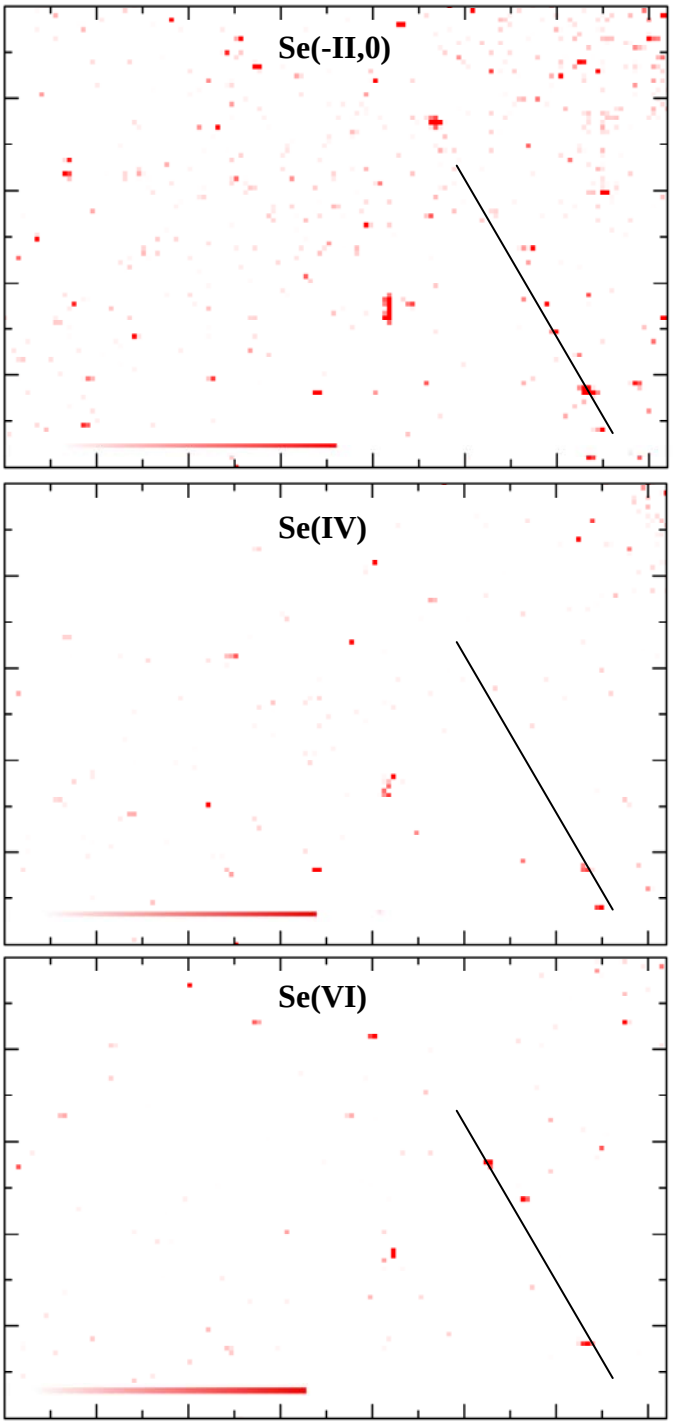

Figure S6. Micro-SXRF maps of sample 09A, 2880 x 2000 µm. Each pixel shows deconvoluted signal (X in equation 3). Se(-II,0) map was collected at 12659.0 eV, Se(IV) at 12663.5 eV, and Se(VI) at 12668.5 eV. Red to white gradient shows decreasing Se levels. The black line is a transect line for which the data is shown in Figure S7.

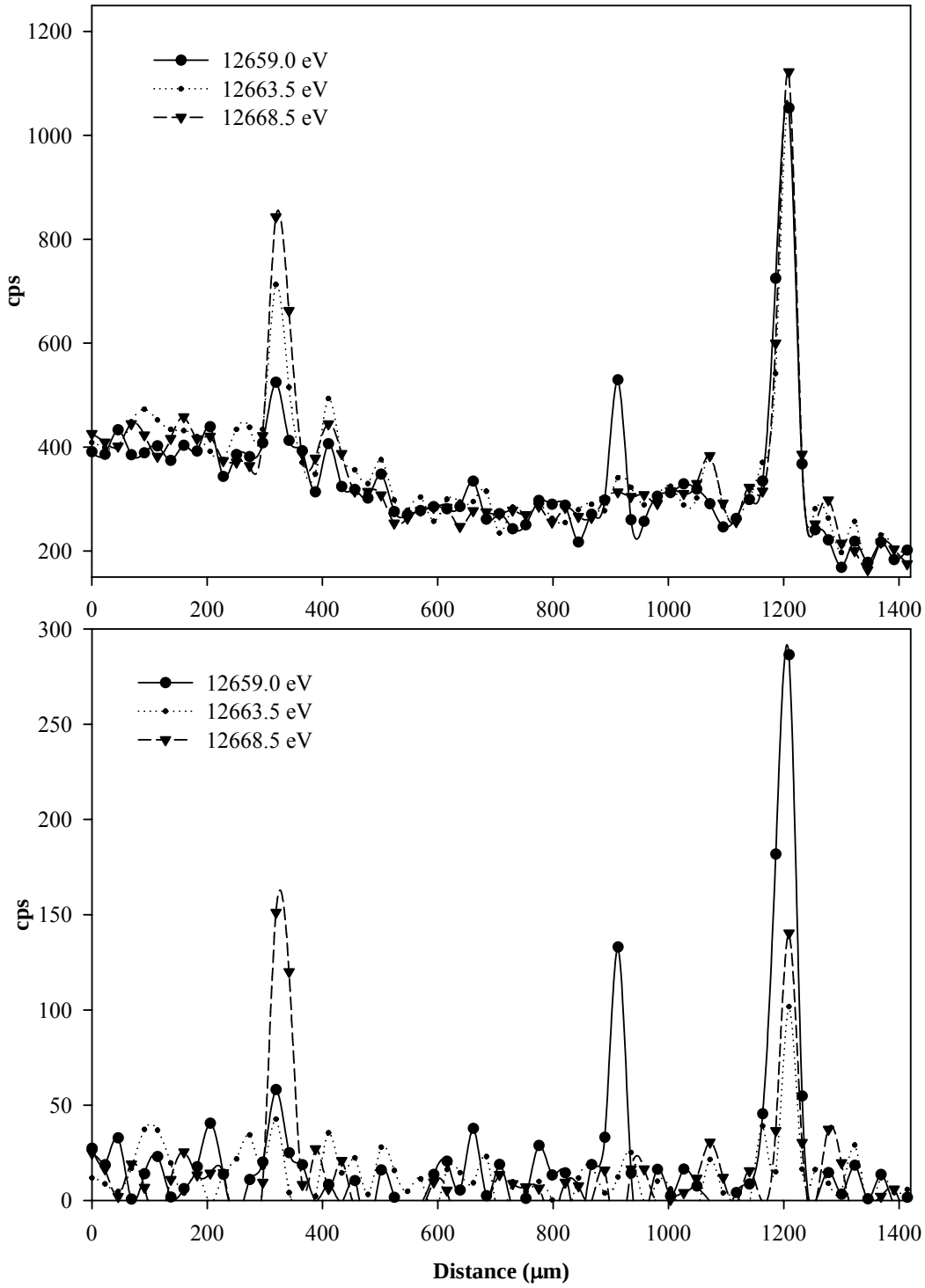

Figure S7. (top) Raw SXRF data (F in equations 4-5) from transect of sample 09A at three energies. (bottom) Signal interference-corrected SXRF data (X in equations 4-5) from transect of sample 04A at three energies. Upper left to lower right of transect correlates with left to right on plot.

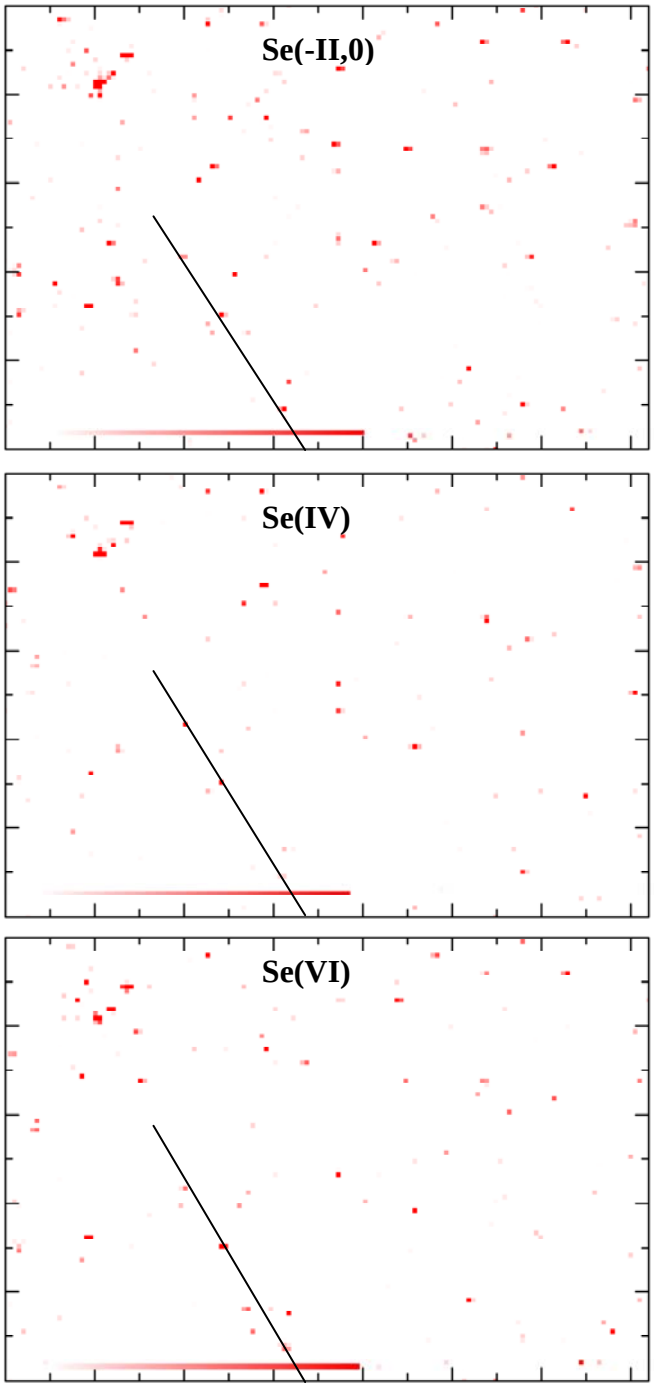

Figure S8. Micro-SXRF maps of sample 09C, 2880 x 2000 µm. Each pixel shows deconvoluted signal (X in equation 3). Se(-II,0) map was collected at 12659.0 eV, Se(IV) at 12663.5 eV, and Se(VI) at 12668.5 eV. Red to white gradient shows decreasing Se levels. The black line is a transect line for which the data is shown in Figure S9.

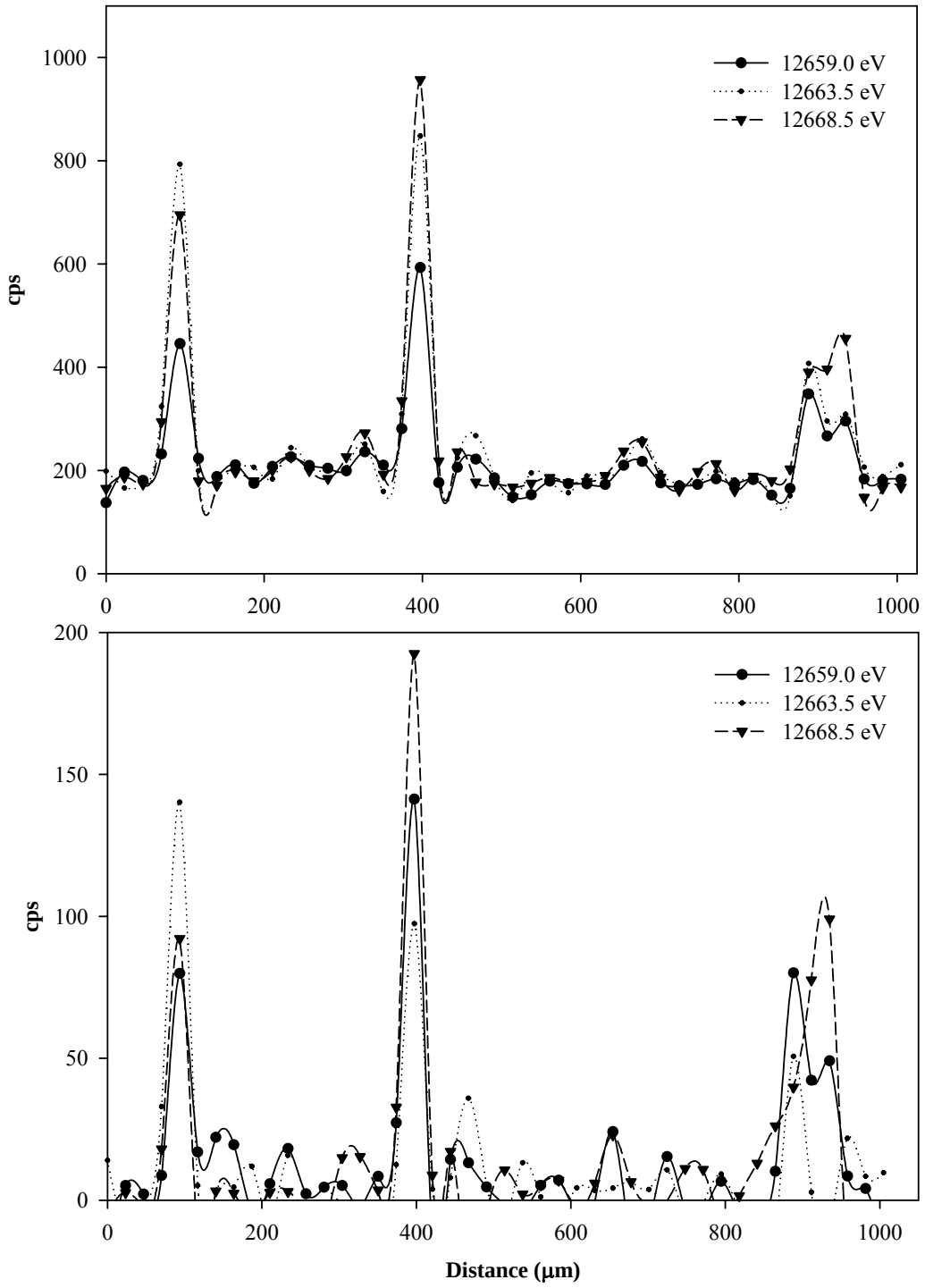

Figure S9. (top) Raw SXRF data (F in equations 4-5) from transect of sample 09C at three energies. (bottom) Signal interference-corrected SXRF data (X in equations 4-5) from transect of sample 04A at three energies. Upper left to lower right of transect correlates with left to right on plot.

Table S3. Average percent ± standard error of each Se species of the total Se intensity for hotspots shown in ternary diagrams (Figure 5). Means across rows are significantly different from each other (p=0.01).

	% Se(-II,0)	% Se(IV)	% Se(VI)
04A n = 415	32 ± 1.3	42 ± 1.4	26 ± 1.4
04G n = 338	30 ± 1.6	44 ± 2.0	25 ± 1.8
09A n = 779	58 ± 1.0	26 ± 0.90	16 ± 0.91
09C n = 405	45 ± 1.5	26 ± 1.4	29 ± 1.4

Literature Cited in Supporting Information

(1) USEPA *Test methods for evaluating solid waste, SW-846, 3rd ed.*; Office of Solid Waste and Emergency Response, 1994.

(2) Kulp, T. R.; Pratt, L. M. Speciation and weathering of selenium in Upper Cretaceous chalk and shale from South Dakota and Wyoming, USA. *Geochim. Cosmochim. Acta* **2004**, *68*, 3687-3701.

(3) Martens, D. A.; Suarez, D. L. Selenium speciation of marine shales, alluvial soils, and evaporation basin soils of California. *J. Environ. Qual.* **1997**, *26*, 424-432.

(4) Wright, M. T.; Parker, D. R.; Amrhein, C. Critical evaluation of the ability of sequential extraction procedures to quantify discrete forms of selenium in sediments and soils. *Environ. Sci. Technol.* **2003**, *37*, 4709 - 4716.

(5) Velinsky, D. J.; Cutter, G. A. Determination of elemental selenium and pyrite-selenium in sediments. *Anal. Chim. Acta* **1990**, *235*, 419-425.

(6) Zhang, Y.; Moore, J. N.; Frankenberger, W. T. Speciation of soluble selenium in agricultural drainage waters and aqueous soil-sediment extracts using hydride generation atomic absorption spectrometry. *Environ. Sci. Technol.* **1999**, *33*, 1652-1656.

(7) Sutton, S. R.; Bajt, S.; Delaney, J.; Schulze, D.; Tokunaga, T. K. Synchrotron x-ray fluorescence microprobe: quantification and mapping of mixed valence state samples using micro-XANES. *Rev. Sci. Instrum.* **1995**, *66*, 1464-1467.

(8) Martens, D. A.; Suarez, D. L. Changes in the distribution of selenium oxidation states with sample storage. *J. Environ. Qual.* **1997**, *26*, 1711-1714.

(9) Ryser, A. L. Biogeochemistry of Selenium in Reclaimed Mine Soils of the Western Phosphate Resource Area In *Plant, Soil, and Entomological Sciences*; University of Idaho: Moscow, ID, 2005; p 154.

(10) Ryser, A. L.; Strawn, D. G.; Marcus, M. A.; Johnson-Maynard, J. L.; Gunter, M. E.; Möller, G. Micro-spectroscopic investigation of selenium-bearing minerals from the Western US Phosphate Resource Area. *Geochem T* **2005**, *6*, 1-11.

(11) Ryser, A. L.; Strawn, D. G.; Marcus, M. A.; Fakra, S.; Johnson-Maynard, J. L.; Möller, G. Microscopically focused synchrotron X-ray investigation of selenium speciation in soils developing on reclaimed mine lands. *Environ. Sci. Technol.* **2006**, *40*, 462-467.

(12) Idaho DEQ *Blackfoot River TMDL waterbody assessment and total maximum daily load*; Idaho Department of Environmental Quality Pocatello Regional Office, 2001.